Acoustic Switch via Kirigami Metasurface

Peizheng Cao,[1,2,†] Wenzhan Ou,[1,2,†] Yingnan Su,[1,2] Yuhang Yin,[3] Erqian Dong,[1,2]
Zhongchang Song,[1,2] Jiafang Li,[4] and Yu Zhang[1,2,*]

[1] *State Key Laboratory of Marine Environmental Science, Xiamen University, Xiamen 361005, China*
[2] *Key Laboratory of Underwater Acoustic Communication and Marine Information Technology of the Ministry of Education, College of Ocean and Earth Sciences, Xiamen University, Xiamen 361005, China*
[3] *Department of Physics, Xiamen University, Xiamen 361005, China*
[4] *School of Physics, Beijing Institute of Technology, Beijing 100081, China*

(Received 3 July 2022; revised 18 August 2022; accepted 2 September 2022; published 15 November 2022)

We design an acoustic switch based on a spiral kirigami metasurface using numerical simulations and evaluate its performance experimentally. By etching an Archimedean spiral on a thin aluminum sheet, a band gap in out-of-plane vibration modes can be generated. The band gap is significantly suppressed by axially stretching the kirigami spiral structure, extending sound propagation to a broader frequency range. The kirigami metasurface is easily deformed and manipulated and can switch the energy transmission *on* and *off* in the desired operating-frequency range, providing an alternative design strategy for acoustic metasurfaces.

DOI: 10.1103/PhysRevApplied.18.054040

I. INTRODUCTION

Metamaterials have been studied extensively over the past few decades for their unique properties, but research on acoustic metamaterials and metasurfaces is currently in the exploration stage. Compared with microwaves and electromagnetic waves, acoustic wavelengths are longer, and most acoustic metamaterials consist of centimeter- or millimeter-scale building-block structures [1–3]. Acoustic metamaterials and metasurfaces are composed of periodically arranged artificial composite structures [4,5]. Traditional acoustic metasurfaces can be categorized based on the structures employed, such as space coiling [6], Helmholtz resonators [7–9], and membranes [10–12]. However, most proposed metasurfaces operate within a narrow frequency band, and their response cannot be tuned after fabrication.

Functional devices, such as acoustic collimators [13–15] and acoustic diodes [16–18], are proposed to exploit the tunable properties of acoustic metamaterials or metasurfaces. Several other metasurface-based strategies are applied to switch the band gaps *on* and *off* [19] by using asymmetric transmission [20,21,53]. Moreover, due to the large amount of surface defects present, the adjustability of the multilayer metasurface is limited by the interlayer separation. This can lead to an extremely small tunable range, which is greatly affected by the resonant frequencies. A recently proposed acoustic switch uses the deformation of an axially adjustable spring to turn sound propagation *on* and *off* over specific frequency ranges [22]. However, the original structure was additively manufactured, and each unit cell was a one-dimensional isotropic helical spiral. Therefore, band regulation from the variation in the duty ratio is limited to two dimensional (2D). Furthermore, most tunable diodes composed of other forms are one-dimensional structures based on the transfer-matrix method, with relatively low tunable sensitivity and size limitations [23–25].

Controlling plate-internal-wave propagation and vibration at low frequencies is challenging. Generally, the formation or suppression of the corresponding bending-wave band gap is investigated using a truss-structure metamaterial [26], also known as a spring-oscillator resonant metamaterial [27–34]. Several interesting structures were also introduced to realize energy harvesting from bending waves and vibration-characteristic detection of bare plates [35–39], but their tunability was relatively poor. Consequently, incorporating simple structures with continuous deformation, such as one-dimensional origami or adjustable beams, would enable the opening and closing of the band gap of bending waves [40,41]. However, it is difficult to achieve continuous wideband adjustment and avoid the influence of the hybrid mode. In addition, prestress is added in the band-gap mode of the control board, which is adjusted by the principle of inertia amplification. It provides the possibility of real-time harmonic modulation propagation. However, the strength of the structure

---

[*] yuzhang@xmu.edu.cn
[†] P. Cao and W. Ou contributed equally to this work.

is relatively high [42]. Here, we investigate the band-gap control of bending waves in a paper-cut structure after acoustic mode conversion using the band structure to overcome these shortcomings.

Kirigami and origami are promising techniques for building three-dimensional (3D) acoustic metasurfaces. They also have potential applications in the field of metamaterials for construction machinery. Various deformation types include a folding metamaterial, a cutting metamaterial, and a mixed-deformation metamaterial (i.e., cutting and folding at the same time). The mechanism of deformation can be explained using mechanics [43]. Combined with scientific and artistic concepts, kirigami enables 3D structures to be formed by stretching 2D-etched patterns. Consequently, kirigami is actively being investigated for the fabrication of functional devices for information storage [44,45], nanophotonics [46–48], microelectromechanical systems [49,50], and elastic wave control [44,51,52,54]. Compared to traditional acoustic metamaterials and metasurfaces, kirigami and origami enable easy and direct shape deformation from 2D substrates to 3D architectures and have remarkable properties, such as adjustable chirality [55]. Therefore, based on their unique transformation functions, kirigami and origami can be used to form 3D acoustic structures that can be arbitrarily rotated and twisted. Herein, we explore the ability of a single-plate substrate transformed into a 3D kirigami metasurface to switch sound propagation *on* and *off*.

II. RESULTS AND DISCUSSION

The kirigami metasurface is manufactured by etching four Archimedean spirals on a homogeneous and structurally tunable aluminum sheet [Fig. 1(a)]. As axial stress is applied to the surface center of the kirigami metasurface, it transforms from a 2D into a 3D structure, changing the acoustic dispersion curve of the metasurface. When the kirigami metasurface is in a flat conformation, it opens a band gap in the out-of-plane (OP) vibration modes and prevents wave propagation. In this condition, the acoustic switch state is in the *off* mode [Fig. 1(b)]. By stretching the kirigami metasurface and deforming it such that the spirals protrude outward, forming a 3D structure, the band gap is inhibited and the wave can propagate in the frequency range of interest [Fig. 1(c)]. In this condition, the switch is in the *on* mode. The proposed kirigami metasurface uses topological deformation to manipulate the propagation of waves in the desired operating-frequency range.

Considering that the topological deformation of the kirigami metasurface requires high ductility, we choose an aluminum sheet (density $\rho = 2700$ kg/m^3, Young's modulus $E = 6.85 \times 10^{10}$ N/m^2, Poisson ratio $\delta = 0.34$) as the substrate material. For all configurations, the lattice constant is $A = 30$ mm and the thickness is $t = 0.5$ mm. The flat kirigami metasurface is constructed by cutting four concentric Archimedean spirals from a homogeneous aluminum sheet with a spiral width of $w = 0.6$ mm [Fig. 1(a)]. The polar representation of the Archimedean spiral is $R = R_0 + b\theta$, where $R_0 = 1$ mm is the inside radius of the spiral, θ is the polar angle, and $b = 8.6/2\pi$ mm rad^{-1} controls the distance between the adjacent spiral curves. The deformation model is derived from finite-element analysis, in which the edges of the unit cell are fixed and the surface center of the unit cell is given an axial displacement of 3 mm [Fig. 1(a)].

To examine the wave-control properties of the proposed kirigami metasurface, the band-structure characteristics are analyzed theoretically. The governing equation for elastic waves propagating in a linear elastic medium is

$$\nabla \cdot [C(\mathbf{r}) \sim \nabla \mathbf{u}(\mathbf{r})] + \rho(\mathbf{r})\omega^2 \mathbf{u}(\mathbf{r}) = 0, \qquad (1)$$

where $\mathbf{r}$ is the position vector; C is the elasticity tensor; $\mathbf{u}$ is the displacement vector; and ρ and ω are the mass density and angular frequency, respectively. For periodic

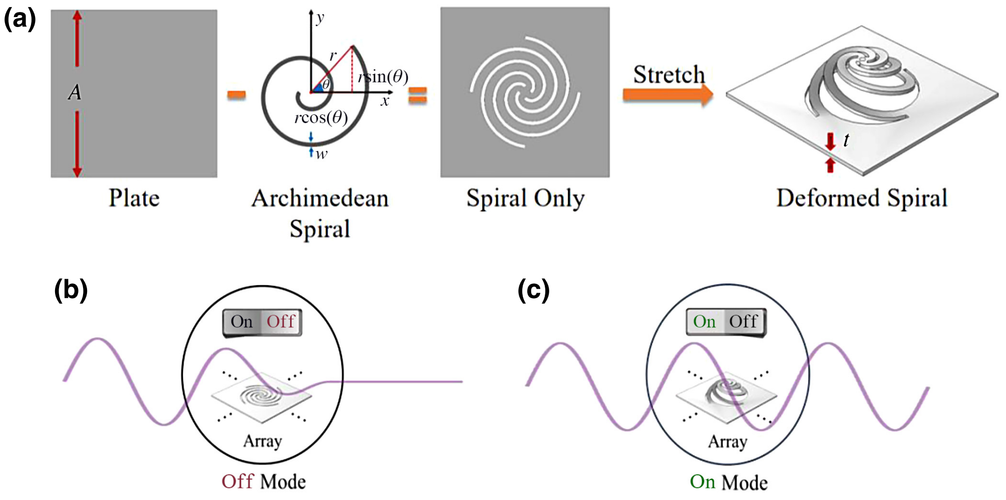

FIG. 1. (a) Preparation and topological deformation of kirigami metasurfaces: four concentric Archimedean spirals are etched on a homogeneous aluminum sheet to form the unit cell of the kirigami metasurface. Stable 3D kirigami structure is formed under axial stress. (b) Acoustic switch in *off* mode inhibits wave propagation. (c) Acoustic switch in *on* mode allows wave propagation.

materials, Bloch's theory can be applied as follows:

$$\mathbf{u}(\mathbf{r}) = \tilde{\mathbf{u}}(\mathbf{r}, \mathbf{k})e^{i(\mathbf{k},\mathbf{r})}, \tag{2}$$

where $\tilde{\mathbf{u}}$ is the Bloch displacement vector, and $\mathbf{k}$ is the wave vector. Equation (1) forms the Bloch eigenvalue problem, which can be solved using the finite-element method. The discrete form of the eigenvalue problem is written as

$$[\mathbf{K} - \omega^2\mathbf{M}]\mathbf{U} = 0, \tag{3}$$

where $\mathbf{K}$ and $\mathbf{M}$ are the stiffness and mass matrices, respectively. $\mathbf{U}$ represents the eigenvector corresponding to the angular frequency ω. The band structures can be calculated by varying k along the Γ-X-M-Γ boundary of the first irreducible Brillouin zone. In this study, COMSOL Multiphysics software (Stockholm, Sweden) is used for numerical simulations.

The band structures of the three types of unit cell are shown in Fig. 2. The introduction of the spiral pattern disrupts the vibration mode of the homogeneous material and opens an OP band gap of 910–1125 Hz [Figs. 2(a) and 2(b)]. As the center of the spiral pattern is axially stretched up to a deformation of 3 mm, the lower limit of the band gap increases until it is equal to the upper frequency limit, resulting in the disappearance of the band

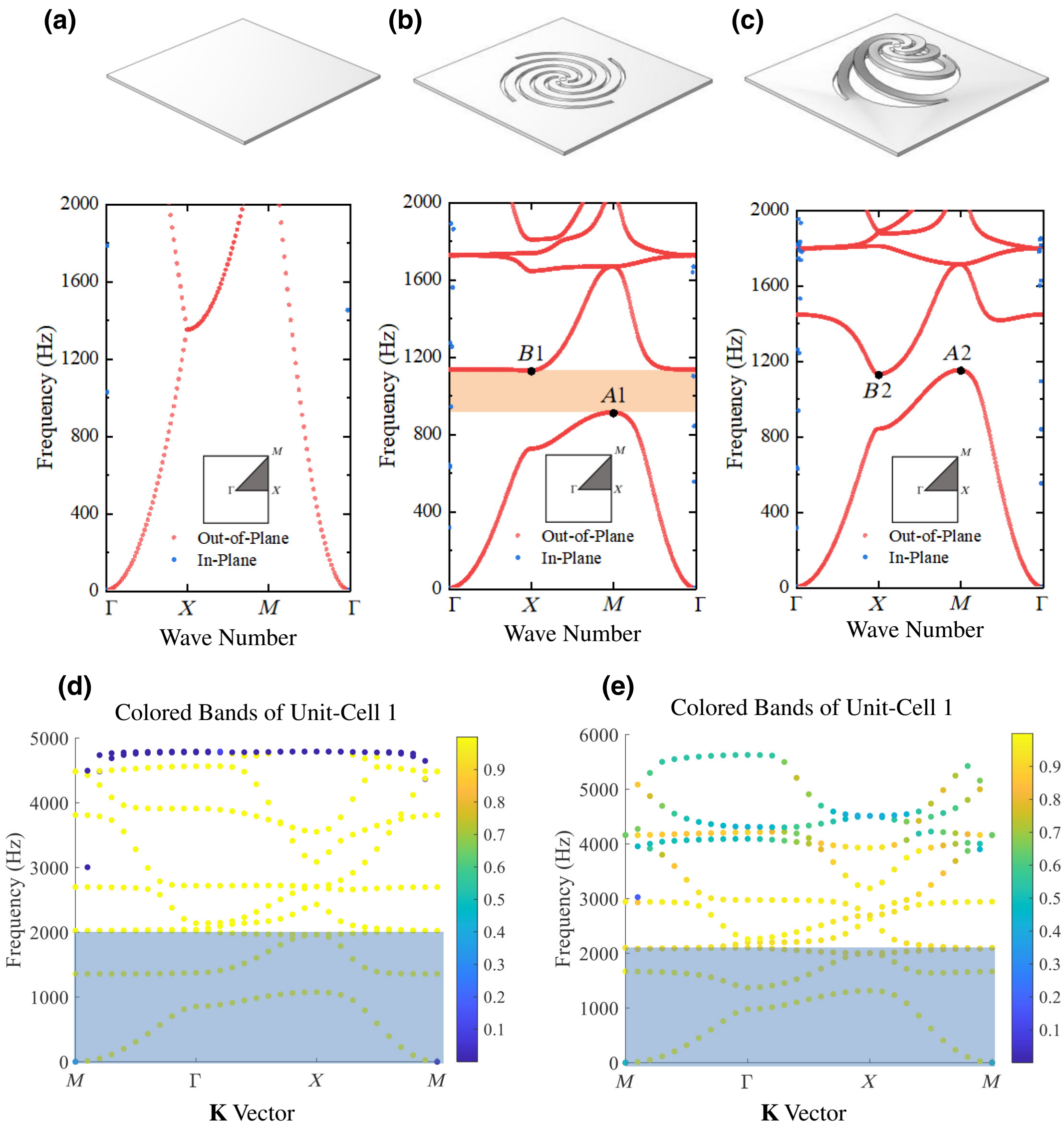

FIG. 2. Band structure of three different unit cells: (a) homogeneous aluminum sheet, (b) kirigami metasurface in the flat state, (c) kirigami metasurface with an axial deformation of 3 mm. Numerical analyses consider wave vectors along the path Γ-X-M-Γ. Band gap of OP vibration modes is shaded in orange, when the kirigami structure (d) is not deformed and (e) is stretched by 3 mm; proportions of in-plane and out-of-plane modes corresponding to the band structure are also shown (the yellower the color, the higher the proportion of out-of-plane mode; the bluer the color, the higher the proportion of in-plane mode).

gap [Fig. 2(c)]. To further reveal the band-structure control mechanism, we compare the vibrational modes of the flat and deformed kirigami metasurfaces. The OP vibration modes at points $A1$, $B1$, $A2$, and $B2$ [see Figs. 2(b) and 2(c) for points] are shown in Fig. 3. Modes $A1$, $A2$, $B1$, and $B2$ represent the characteristics at the lower and upper edges of the band structure, respectively.

In addition, there is a Shear wave mode in the kirigami structure, but the influence of an in-plane shear mode is not dominant. As shown in Figs. 2(d) and 2(e), the more yellow the color, the more out-of-plane modes the whole mode consists of. The bluer the band color, the more in-plane displacements the pattern contains. However, the frequency band studied in this paper is in the range of 0–2000 Hz (blue shaded area), and the out-of-plane mode is mainly shown in the figure. In summary, the influence of in-plane modes is not considered in this paper.

To study the band-control mechanism of the kirigami structure, frequency points $A1$ and $A2$ correspond to the downstream frequencies of the kirigami deformation, while $B1$ and $B2$ correspond to the upstream frequencies (Fig. 2). The modes of vibration at frequencies corresponding to the sweep direction of points $B1$ and $B2$ are consistent before and after deformation (Figs. 2 and 3). In the in-plate mode, the wave propagation is stable. The uplink frequency of the total band gap remains unchanged. The frequency points corresponding to the energy band points of $A1$ and $A2$ show that the downlink frequency increases with kirigami stretching by 3 mm, causing the band gap to disappear and reach the open state. According to the mode diagram in Fig. 3(a), the difference between the downlink frequency ($A1$, $A2$) and uplink frequency ($B1$, $B2$) is that the vibration of the downlink frequency ($A1$, $A2$) is concentrated in the kirigami structure. We examine the stress distribution of the kirigami structure in detail [Fig. 3(b)]. Without deformation, stress is concentrated at the endpoints of the spiral etching. The kirigami structure can be considered part of a spring oscillator, and deformation destroys Lamb-wave transmission. When the elastic coefficient increases, the vibration resonance of the kirigami structure prevents energy transmission, creating a band gap. Point $A2$ corresponds to the downlink frequency at an axial deformation of 3 mm. When the wave is transmitted from the kirigami structure, the stress distribution is confined to the edges of the kirigami structure [Fig. 3(b) mode $A2$]. The kirigami deformation forms a three-legged tower structure. Compared with the change for an ordinary spring, the elastic coefficient of the kirigami structure decreases, and its structural stability is better than that without deformation after excitation. Therefore, the frequency value at the end of the X-M direction will increase [Figs. 2(b) and 2(c)], so that the band gap disappears, and the kirigami structure is in the *on* state. These results indicate that the deformation of the kirigami structure can effectively regulate the transmission of in-plate waves.

The spiral pattern renders kirigami drawing characteristics to the model, enabling the band gap to be adjusted from closed to open by modifying the degree of 3D deformation of the kirigami structure. The band-gap characteristics can be extracted to facilitate the study of the rule. We can see in Fig. 2 that the spiral curves introduce a wide band gap compared to the plate. As can be seen in Fig. 4(a), the change of band gaps 1–4 shows that the control-band structure (band-gap width) of the kirigami deformation decreases as the deformation degree increases. We extract the band gap of the uplink and downlink frequency for further quantitative analyses. Figure 4(b) shows that, as the deformation height increases, the uplink frequency (1125 Hz) remains constant, while the downlink frequency increases exponentially from 910 Hz until the deformation

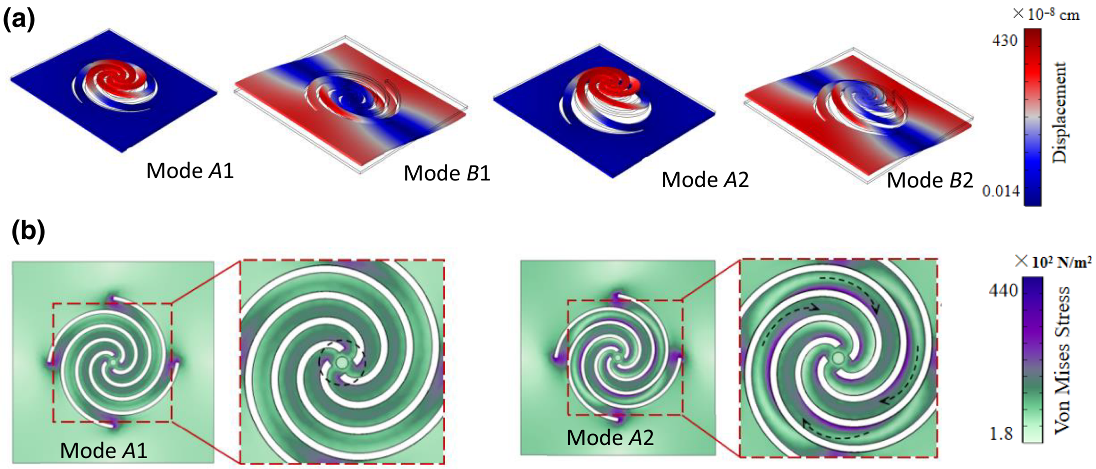

FIG. 3. Comparison of mode shapes around the band gap: (a) displacement-mode shapes (at points $A1$, $A2$, $B1$ and $B2$) and (b) mode stress-mode shapes (at points $A1$ and $A2$) [selection of points is shown in FIG. 2(b) and 2(c)].

height exceeds more than 2.8 mm, at which point the uplink and downlink frequencies overlap and the band gap disappears. Foehr *et al.* conducted a study in the subwavelength frequency range (below the Bragg-scattering limit) [54]. Similarly, even if the kirigami structure in this paper is deformed to the maximum, its ratio to the minimum wavelength is less than one thousandth, so it still meets the definition of subwavelength. Figure 4(c) shows the relationship between the normalized band-gap width and the deformation height, with $y = -78.18\exp(0.4907x) + 79.18$, after curve fitting. Therefore, the band-gap width varies continuously and exponentially with the deformation size.

To experimentally verify the wave-energy control function of the acoustic switch, we fabricate an acoustic switch consisting of a quasiperiodic array of 7×7 unit cells (Fig. 5). The dimensions of the fabricated structure are $270 \times 270 \times 0.5$ mm^3. Butyl glue is used to section the edges of the fabricated structure to weaken the influence of the rigid boundary. The experimental setup is illustrated in Fig. 5(a). The excitation signal produced by a personal computer (PC) is fed to a loudspeaker through a signal amplifier, and the excitation point is at point E. A laser Doppler vibrometer (Polytec OFV-505 with an OFV-5000 decoder) is used to detect the traveling-wave velocity at measurement-point M. Velocity data are collected using the PC through a data acquisition card.

To facilitate measurement and clamping, we set aside a 30-mm nonkirigami-etched range around the model and put blue butyl glue around it. Therefore, the influence of the rigid boundary is weakened during the experimental measurement to guarantee the accuracy of the results. However, owing to the experimental environment, errors are inevitable.

A frequency of 600 to 1450 Hz with a step size of 3 Hz is examined, and the measurement results are processed to obtain the dispersion curve [Fig. 5(e)]. The transmission ratio is defined as follows:

$$\xi = \frac{{a_1}^2}{{a_2}^2}, \tag{4}$$

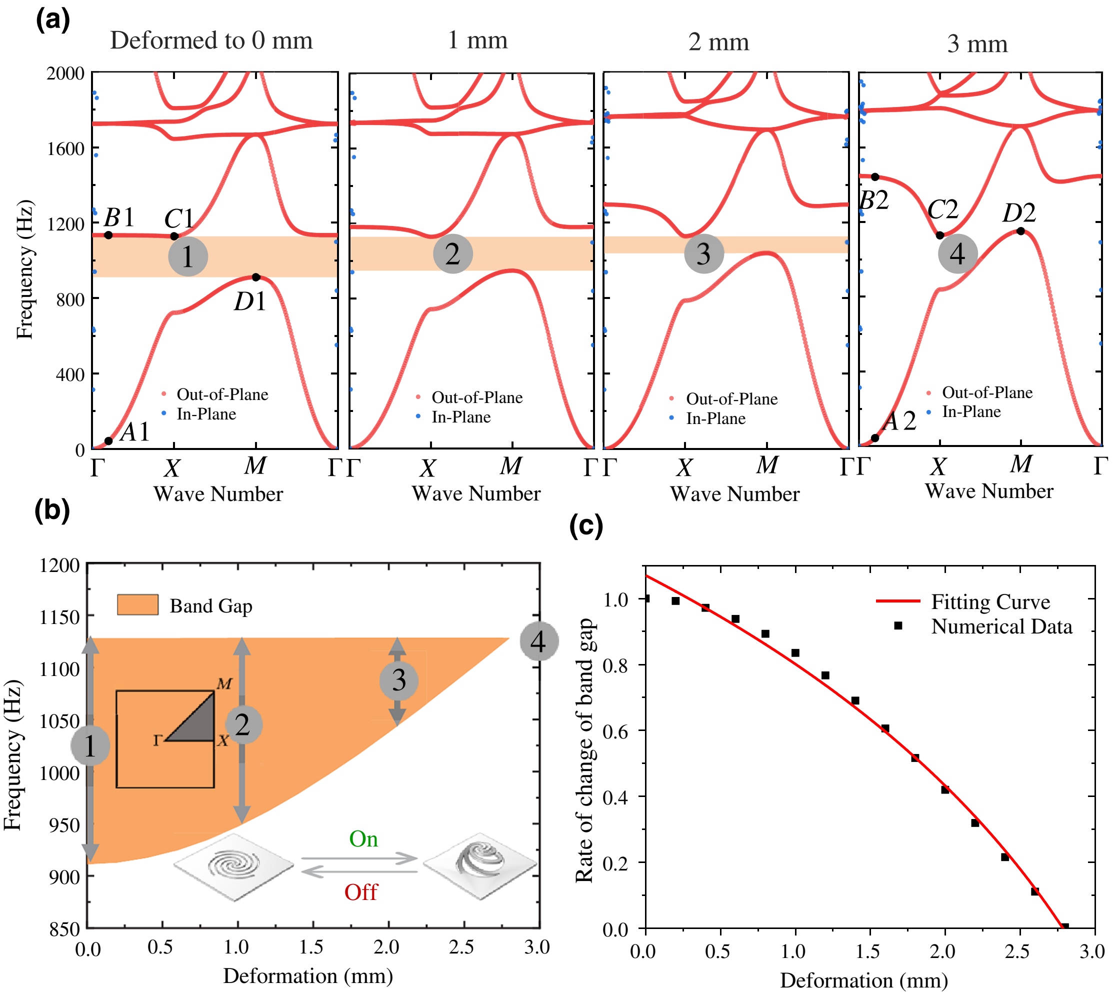

FIG. 4. (a) Influence of different deformation degrees on band regulation. (b) Upstream and downstream frequencies corresponding to different deformation degrees. (c) Fitting diagram of deformation and band width.

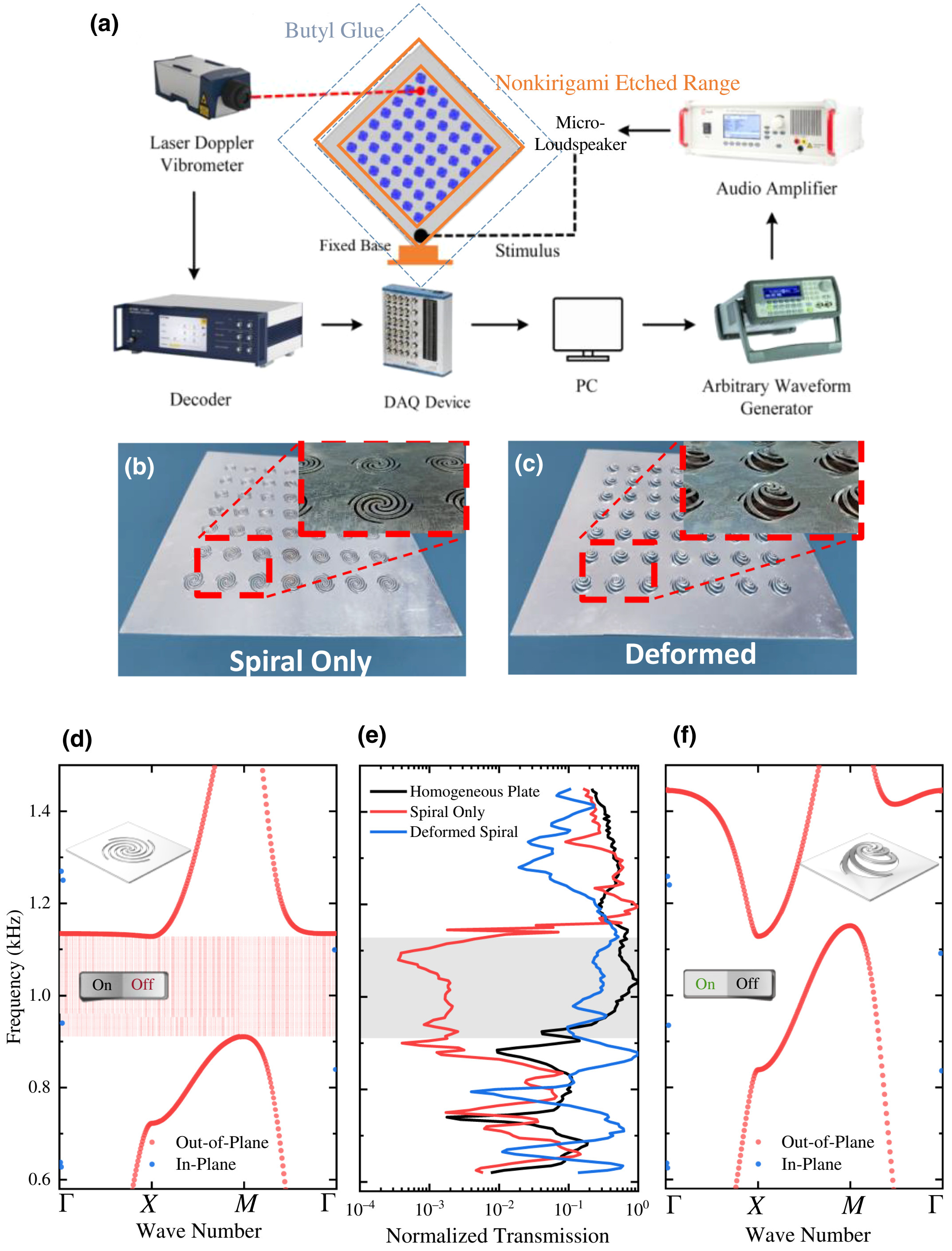

FIG. 5. (a) Experimental setup schematic diagram. (b) Acoustic switch composed of an array of 7 × 7 flat unit cells. (c) Acoustic switch composed of an array of 7 × 7 deformed unit cells. Experimental and numerical characterization of wave propagation through the acoustic switch. (d) *Off* -mode band structure of the acoustic switch. (e) Measured frequency response. Black line for homogeneous aluminum sheet as a reference, and red and blue lines for *off* and *on* modes of the acoustic switch, respectively. (f) *On*-mode band structure of the acoustic switch.

where a_1 is the received signal and a_2 is the output signal. The gray part in Fig. 5(e) represents the band gap, which corresponds to the red band gap in Fig. 5(d). By comparing the results, we find that the band gap of the unstretched kirigami structure [corresponding to the red line in Fig. 5(e)] matches the theoretical range of 910 to 1125 Hz with a slight deviation. The deviation is mainly affected by the processing error of the kirigami structure and the boundary conditions of the opposite internal-wave propagation. A theoretical analysis of the out-of-plane waveband structure can explain this phenomenon. There are also in-plane wave results in the band diagram [blue dots in Figs. 5(d) and 5(f)], but it is beyond the analysis-frequency band, so it has little influence on the results. Moreover, according to the long-wave approximation, elastic waves and acoustic waves are inevitably unified. According to our theoretical derivation, if stretching is not applied [Fig. 5(d)], negative parameters appear in both k_x and k_y, resulting in a full band gap of 910–1125 Hz, corresponding to the *off* mode. When stretching is applied along the axis, the kirigami structure switches to the *on* mode, as shown in Fig. 5(f). The structure is not stretched (red line) compared with other experimental results, and it is found that, in the same frequency band (910–1125 Hz), its transmittance is 1–2 orders of magnitude lower than that of other frequency bands, reaching 10^{-3} at the lowest. Therefore, in this case, the band gap can be estimated theoretically, which verifies the *off* effect. Corresponding to the control experimental results [Fig. 5(e)], the black line represents the result for the flat plate and the blue line shows the *on* state due to deformation. The black and blue lines have slight differences. This indicates that the kirigami structure controls the in-plate propagation mode. As discussed above, the kirigami structure eliminates the influence of the band gap.

III. CONCLUSION

A 3D acoustic switch based on a kirigami metasurface is proposed, and its acoustic characteristics are examined through numerical simulations and experiments. The results show that an external force on the kirigami structure produces a linear deformation, affecting wave transmission at the subwavelength scale. Deformation enables switching between the 2D and 3D modes, as well as band-gap tunability over a wide band range. Our study and its results can be adapted to a wide range of applications, such as information encoding, encrypted communication, and miniaturized tunable devices.

ACKNOWLEDGMENTS

We would like to thank Professor Christ and Liwang Liu from KU Leuven for useful discussions. We also want to thank Yangyang Zhou, Jinhu Zhang, and Mengting Lin from Xiamen University for their helpful assistance with our experiments. This work is supported by the National Natural Science Foundation of China (Grants No. 12074323 and 42106181); the Special Fund for Marine and Fishery Development of Xiamen (Grant No. 20CZB015HJ01); the Water Conservancy Science and Technology Innovation Project of Guangdong (Grant No. 2020-16); the Major Science and Technology Project of Fujian (Grant No. 2021NZ033016); and the Outstanding Postdoctoral Scholarship, State Key Laboratory of Marine Environmental Science at Xiamen University.

[1] B. Popa and S. Cummer, Non-reciprocal and highly nonlinear active acoustic metamaterials, Nat. Commun. **5**, 1 (2014).

[2] B. Popa, D. Shinde, A. Konneker, and S. Cummer, Active acoustic metamaterials reconfigurable in real-time, Phys. Rev. B. **91**, 22 (2015).

[3] K. Yu, N. Fang, G. Huang, and Q. Wang, Magnetoactive acoustic metamaterials, Adv. Mater. **30**, 21 (2018).

[4] Y. Xie, W. Wang, H. Chen, A. Konneker, B. Popa, and S. Cummer, Wavefront modulation and subwavelength diffractive acoustics with an acoustic metasurface, Nat. Commun. **5**, 1 (2014).

[5] N. Yu, P. Genevet, M. A. Kate, F. Aieta, J. P. Tetienne, F. Capasso, and Z. Gaburro, Light propagation with phase discontinuities: Generalized laws of reflection and refraction, Science **334**, 333 (2011).

[6] R. Ghaffarivardavagh, J. Nikolajczyk, R. Glynn Holt, S. Anderson, and X. Zhang, Horn-like space-coiling metamaterials toward simultaneous phase and amplitude modulation, Nat. Commun. **9**, 1349 (2018).

[7] W. Cao, C. Zhang, L. Wu, K. Guo, J. Ke, T. Cui, and Q. Cheng, Tunable Acoustic Metasurface for Three-Dimensional Wave Manipulations, Phys. Rev. Appl. **15**, 2 (2021).

[8] Y. Zhang, H. Cheng, J. Tian, and S. Chen, Frequency-Selected Bifunctional Coding Acoustic Metasurfaces, Phys. Rev. Appl. **14**, 6 (2020).

[9] J. Guo, X. Zhang, Y. Fang, and Z. Jiang, A compact low-frequency sound-absorbing metasurface constructed by resonator with embedded spiral neck, Appl. Phys. Lett. **117**, 221902 (2020).

[10] J. Lan, X. Zhang, X. Liu, and Y. Li, Wavefront manipulation based on transmissive acoustic metasurface with membrane-type hybrid structure, Sci. Rep. **8**, 1 (2018).

[11] P. Liu, X. Chen, W. Xu, and Y. Pei, Magnetically controlled multifunctional membrane acoustic metasurface, J. Appl. Phys. **127**, 18 (2020).

[12] Y. Tang, B. Liang, J. Yang, and J. Chen, Voltage-controlled membrane-type active acoustic metasurfaces with ultrathin thickness, Appl. Phys. Express **12**, 064501 (2019).

[13] W. Liu and X. Su, Collimation and enhancement of elastic transverse waves in two-dimensional solid phononic crystals, Phys. Lett. A **374**, 29 (2010).

[14] J. Shi, S. Lin, and T. Huang, Wide-band acoustic collimating by phononic crystal composites, Appl. Phys. Lett. **92**, 111901 (2008).

[15] L. Zhao, T. Horiuchi, and M. Yu, Broadband acoustic collimation and focusing using reduced aberration acoustic Luneburg lens, J. Appl. Phys. **130**, 21 (2021).

[16] S. Raval, K. Petrover, and A. Baz, Experimental characterization of a one-dimensional nonreciprocal acoustic metamaterial with anti-parallel diodes, J. Appl. Phys. **129**, 7 (2021).

[17] A. Baz, Active nonreciprocal acoustic metamaterials using a switching controller, J. Acoust. Soc. Am. **143**, 1376 (2018).

[18] C. Fu, B. Wang, T. Zhao, and C. Chen, High efficiency and broadband acoustic diodes, Appl. Phys. Lett. **112**, 051902 (2018).

[19] Z. Gu, X. Fang, T. Liu, H. Gao, S. Liang, Y. Li, B. Liang, J. Cheng, and J. Zhu, Tunable asymmetric acoustic

transmission via binary metasurface and zero-index metamaterials, Appl. Phys. Lett. **118**, 113501 (2021).

[20] S. Zhang, Y. Zhang, W. Lu, B. Xu, and Y. Zhang, Subwavelength asymmetric transmission device for acoustic waves with multiple incident directions, J. Phys. D: Appl. Phys. **52**, 29 (2019).

[21] S. Tang, B. Ren, Y. Feng, J. Song, and Y. Jiang, Broadband controllable asymmetric accelerating beam via bilayer binary acoustic metasurfaces, Ann. Phys. **534**, 2 (2021).

[22] S. Babaee, N. Viard, P. Wang, N. Fang, and K. Bertoldi, Harnessing deformation to switch on and off the propagation of sound, Adv. Mater. **28**, 8 (2016).

[23] Z. Li, Y. Wang, and Y. Wang, Electro-mechanical coupling diode of elastic wave in nonlinear piezoelectric metamaterials, J. Acoust. Soc. Am. **150**, 891 (2021).

[24] A. Gliozzi, M. Miniaci, A. Krushynska, B. Morvan, M. Scalerandi, N. M. Pugno, and F. Bosia, Proof of concept of a frequency-preserving and time-invariant metamaterial-based nonlinear acoustic diode, Sci. Rep. **9**, 9560 (2019).

[25] Z. Li, Y. Wang, and Y. Wang, Tunable mechanical diode of nonlinear elastic metamaterials induced by imperfect interface, Proc. R. Soc. A **477**, 20200357 (2021).

[26] Z. Guo, G. Hu, V. Sorokin, L. Tang, X. Yang, and J. Zhang, Low-frequency flexural wave attenuation in metamaterial sandwich beam with hourglass lattice truss core, Wave Motion **104**, 102750 (2021).

[27] F. He, Z. Shi, D. Qian, J. Tu, and M. Chen, Flexural wave bandgap properties in metamaterial dual-beam structure, Phys. Lett. A **429**, 127950 (2022).

[28] D. Yao, M. Xiong, J. Luo, and L. Yao, Flexural wave mitigation in metamaterial cylindrical curved shells with periodic graded arrays of multi-resonator, Mech. Syst. Signal Process. **168**, 108721 (2022).

[29] C. Cai, J. Zhou, K. Wang, H. Pan, D. Tan, D. Xu, and G. Wen, Flexural wave attenuation by metamaterial beam with compliant quasi-zero-stiffness resonators, Mech. Syst. Signal Process. **174**, 109119 (2022).

[30] J. Miranda and J. Dos Santos, Flexural wave band gaps in multi-resonator elastic metamaterial Timoshenko beams, Wave Motion **91**, 102391 (2019).

[31] J. Miranda, S. Rodrigues, J. Aranas, and J. Dos Santos, Plane wave expansion and extended plane wave expansion formulations for Mindlin-Reissner elastic metamaterial thick plates, J. Math. Anal. Appl. **505**, 2 (2022).

[32] J. Miranda, E. Nobrega, A. Ferreira, and J. Dos Santos, Flexural wave band gaps in a multi-resonator elastic metamaterial plate using Kirchhoff-Love theory, Mech. Syst. Signal Process. **116**, 480504 (2019).

[33] T. Wang, M. Sheng, Z. Guo, and Q. Qin, Flexural wave suppression by an acoustic metamaterial plate, Appl. Acoust. **114**, 118124 (2016).

[34] J. Jung and S. Wang, Investigation of flexural wave band gaps in a locally resonant metamaterial with plate-like resonators, Wave Motion **93**, 102492 (2020).

[35] S. Zouari, J. Brocail, and J.-M. Génevaux, Flexural wave band gaps in metamaterial plates: A numerical and experimental study from infinite to finite models, J. Sound Vib. **435**, 2462636 (2018).

[36] T. Ma, Q. Fan, Z. Li, C. Zhang, and Y. Wang, Flexural wave energy harvesting by multi-mode elastic metamaterial cavities, Extreme Mech. Lett. **41**, 101073 (2020).

[37] L. Ning, Y. Wang, and Y. Wang, Active control of a black hole or concentrator for flexural waves in an elastic metamaterial plate, Mech. Mater. **142**, 103300 (2020).

[38] L. Ning, Y. Wang, and Y. Wang, Active control cloak of the elastic wave metamaterial, Int. J. Solids Struct. **202**, 126125 (2020).

[39] H. Zhu and F. Semperlotti, Phononic thin plates with embedded acoustic black holes, Phys. Rev. B **91**, 10 (2015).

[40] Z. Xu, S. Xu, and K. Chuang, Coupled flexural-longitudinal waves in an origami metamaterial with uncoupled creases, Phys. Rev. A **396**, 127232 (2021).

[41] W. Zhou, W. Chen, Z. Chen, and C. Lim, Actively controllable flexural wave band gaps in beam-type acoustic metamaterials with shunted piezoelectric patches, Eur. J. Mech. A **77**, 103807 (2019).

[42] M. Miniaci, M. Mazzotti, A. Amendola, and F. Fraternali, Effect of prestress on phononic band gaps induced by inertial amplification, Int. J. Solids Struct. **216**, 156166 (2021).

[43] Z. Zhai, L. Wu, and H. Jiang, Mechanical metamaterials based on origami and kirigami, Appl. Phys. Rev. **8**, 041319 (2021).

[44] O. Bilal, A. Foehr, and C. Daraio, Reprogrammable phononic metasurfaces, Adv. Mater. **29**, 39 (2017).

[45] J. Hannu and H. Jantunen, Kirigami-inspired dual-parameter tactile sensor with ultrahigh sensitivity, multimodal and strain-insensitive features, Flexible Printed Electron. **6**, 034005 (2021).

[46] J. Majors, Kirigami brings new dimensions of cutting-edge nanophotonics to ion beam patterning, Scilight **2018**, 38 (2018).

[47] J. Li and Z. Liu, Focused-ion-beam-based nano-kirigami: From art to photonics, Nanophotonics **7**, 10 (2018).

[48] Z. Liu, H. Du, J. Li, L. Lu, and N. Fang, Nano-kirigami with giant optical chirality, Sci. Adv. **4**, 7 (2018).

[49] A. Baldwin and E. Meng, Kirigami strain sensors microfabricated from thin-film parylene C, J. Microelectromech. Syst. **27**, 6 (2018).

[50] X. Ning, X. Wang, Y. Zhang, X. Yu, D. Choi, N. Zhang, D. Kim, and Y. Huang, Assembly of advanced materials into 3D functional structures by methods inspired by origami and kirigami: A review, Adv. Mater. Interfaces **5**, 13 (2018).

[51] T. Jiang and Q. He, Dual-directionally tunable metamaterial for low-frequency vibration isolation, Appl. Phys. Lett. **110**, 021907 (2017).

[52] R. Zhu, H. Yasuda, G. Huang, and J. Yang, Kirigami-based elastic metamaterials with anisotropic mass density for subwavelength flexural wave control, Sci. Rep. **8**, 1 (2018).

[53] P. Cao, Y. Zhang, S. Zhang, W. Ou, and N. Fang, Switching Acoustic Propagation via Underwater Metasurface, Phys. Rev. Appl. **13**, 4 (2020).

[54] A. Foehr, O. Bilal, S. Huber, and C. Daraio, Spiral-Based Phononic Plates: From Wave Beaming to Topological Insulators, Phys. Rev. Lett. **120**, 205501 (2018).

[55] Z. Wang, L. Jing, K. Yao, Y. Yang, B. Zheng, C. M. Soukoulis, H. Chen, and Y. Liu, Origami-based reconfigurable metamaterials for tunable chirality, Adv. Mater. **29**, 1700412 (2017).